Coversheet for "High-Tide Floods and Storm Surges During Atmospheric Rivers on the US West Coast'

Christopher G. Piecuch[1,†], Sloan Coats[2], Sönke Dangendorf[3], Felix W. Landerer[4], J. T. Reager[4], Philip R. Thompson[2], and Thomas Wahl[5]

[1] *Woods Hole Oceanographic Institution, Woods Hole, Massachusetts, USA*

[2] *University of Hawai'i at Mānoa, Honolulu, HI, USA*

[3] *Old Dominion University, Norfolk, VA, USA*

[4] *Jet Propulsion Laboratory, California Institute of Technology, Pasadena, CA, USA*

[5] *University of Central Florida, Orlando, FL, USA*

† cpiecuch@whoi.edu

High-Tide Floods and Storm Surges During Atmospheric Rivers on the US West Coast

Christopher G. Piecuch[1], Sloan Coats[2], Sönke Dangendorf[3], Felix W. Landerer[4], J. T. Reager[4], Philip R. Thompson[2], and Thomas Wahl[5]

Christopher G. Piecuch, Woods Hole Oceanographic Institution, 266 Woods Hole Road, Woods Hole, MA 02543, USA. (cpiecuch@whoi.edu)

[1]Woods Hole Oceanographic Institution, Woods Hole, MA, USA.

[2]University of Hawai'i at Mānoa, Honolulu, HI, USA.

[3]Old Dominion University, Norfolk, VA, USA

[4]Jet Propulsion Laboratory, California Institute of Technology, Pasadena, CA, USA.

[5]University of Central Florida, Orlando, FL, USA.

Abstract. Atmospheric rivers (ARs) effect inland hydrological impacts related to extreme precipitation. However, little is known about the possible coastal hazards associated with these events. Here we elucidate high-tide floods (HTFs) and storm surges during ARs on the US West Coast during 1980–2016. HTFs and landfalling ARs co-occur more often than expected from random chance. Between 10%–63% of HTFs coincide with landfalling ARs, depending on location. However, only 2%–15% of ARs coincide with HTFs, suggesting that ARs typically must co-occur with anomalously high tides or mean sea levels to cause HTFs. Storm surges during ARs are interpretable in terms of local wind, pressure, and precipitation forcing: meridional wind and barometric pressure are the primary drivers of storm surge, but precipitation can also make secondary contributions. This study highlights the relevance of ARs to coastal impacts, clarifies the drivers of storm surge during ARs, and identifies future research directions.

Plain Language Summary. ARs drive hydrological hazards over land related to extreme precipitation. As they make landfall, ARs typically bring heavy rains, strong winds, and low pressures to the coast. While these factors can cause storm surge and coastal flooding, little attention has been paid to possible coastal impacts of ARs. We establish relationships between ARs and HTFs on the US West Coast and identify the factors causing storm surge during ARs. HTFs occur at nearly the same time that ARs make landfall more often than expected from chance, meaning that ARs contribute importantly to HTFs. Even so, few ARs lead to HTFs—favorable tides or mean sea-level anomalies are usually needed on top of the storm surge from an AR to cause a HTF. Storm surge during an AR can be explained by the heavy rain, strong wind, and low pressure typically associated with the event; wind and pressure are the primary factors causing the surge, but rainfall can also have a secondary influence. Our results highlight how HTFs arise from the subtle interweaving of storm surge, tide, and mean sea-level effects, thus providing important information to managers and modelers, and motivating future studies on relationships between ARs and coastal hazards globally.

Key Points:

- HTFs on the US West Coast co-occur with landfalling ARs more often than expected from random chance.
- Between 10%–63% of HTFs observed by tide gauges coincide with landfalling ARs, depending on location.
- Meridional wind and barometric pressure make primary contributions to storm surge during ARs, but rainfall can also have a secondary effect.

1. Introduction

Atmospheric rivers (ARs) are long, narrow filaments of strong horizontal water vapor transport in the lower troposphere, typically associated with cold fronts of extratropical cyclones (Cordeira et al., 2013; Ralph et al., 2004; Ralph et al., 2017). ARs play an important role in the hydrological cycle, accomplishing most of the poleward moisture transport in the atmosphere at midlatitudes (Newman et al., 2012; Zhu and Newell, 1998). Landfalling ARs can be forced upwards by orography, leading to extreme precipitation and a range of hydrological impacts (Neiman et al., 2008). In California, for example, precipitation due to ARs has ended droughts and caused floods, landslides, and other debris flows (Dettinger, 2013; Du et al., 2018; Hendy et al., 2015; Oakley et al., 2017; Oakley et al., 2018; Ralph et al., 2013; Wang et al., 2017; White et al., 2019).

While most studies of hazards related to ARs focus on hydrological impacts (Payne et al., 2020), the conditions typifying ARs—heavy rain, strong wind, low pressure—also drive storm surge at the coast (Gill, 1982; Pugh and Woodworth, 2014). This suggests

that ARs could be relevant to coastal impacts, such as high-tide floods (HTFs; Moftakhari et al., 2018; Sweet and Park, 2014; Sweet et al., 2021), which negatively affect transportation, property, and public health and safety (Hino et al., 2019; Moftakhari et al., 2017). The frequency of HTFs along the US West Coast has increased in recent decades in some places (San Diego, La Jolla, San Francisco, and Seattle), and more generally shows interannual variability that correlates with phases of the El Niño-Southern Oscillation (ENSO; Sweet et al., 2021). However, few studies investigate the relationship between coastal sea level and ARs.

Khouakhi and Villarini (2016) quantify the correspondence between ARs and extreme sea-level statistics on the US West Coast. They find that annual maxima of hourly still water levels at tide gauges between San Diego, California and Tofino, British Columbia occur within 12 hours of passing ARs 15–50% of the time. These authors also determine a relationship with modes of large-scale climate variability. For example, exceedances over the 99.5th percentile of the hourly still water level distribution during ARs occur more frequently during El Niños and less frequently during La Niñas.

Shinoda et al. (2019) study the oceanic response to ARs during the CalWater 2015 field campaign. They observe daily averaged still water level anomalies of 30–50 cm at the Neah Bay, Washington and South Beach, Oregon tide gauges coinciding with landfalling ARs on 16th January and 6th February 2015. These authors determine that a high-resolution ocean general circulation model reproduces the timing of observed storm surges, but only about half of their magnitude. Shinoda et al. (2019) posit that

the storm-surge response is mainly due to alongshore winds and coastal currents, and that model-data discrepancies reflect small-scale processes unresolved by the model.

These studies advance understanding of ARs and their impacts on sea level, but they also imply outstanding questions. First, the relationship between ARs and coastal impacts remains unclear. For instance, annual-maxima and peaks-over-threshold statistics from Khouakhi and Villarini (2016) are not necessarily informative of HTFs. Annual maxima do not correspond to HTFs in years without HTFs, and this statistic overlooks HTFs during years with multiple HTFs. Likewise, the 99.5th percentile of a still water level distribution usually does not correspond to, and tends to be lower than, impact thresholds (Table S1; Sweet et al., 2018), meaning that many peaks over thresholds studied by Khouakhi and Villarini (2016) do not correspond to HTFs. Second, the factors driving storm surge during ARs remain to be established. For example, Shinoda et al. (2019) interpret storm surges during ARs in terms of the ocean's dynamic response to wind forcing. Their interpretation contrasts with Bromirski et al. (2017), who reason that the ocean's isostatic adjustment to barometric pressure is the primary mechanism of storm surge along the US West Coast. Khouakhi and Villarini (2016) recommend a future study to clarify the roles of wind and pressure forcing on storm surges during ARs.

Here we address these outstanding questions related to ARs, HTFs, and storm surges on the US West Coast. We consider tide-gauge data, HTF thresholds, a catalog of ARs, and a gridded atmospheric reanalysis to establish the relationship between ARs and HTFs as well as the factors forcing storm surge during ARs. Results reveal that ARs

contribute significantly to HTFs on the US West Coast, and clarify the relative effects of wind, pressure, and precipitation forcing on the associated storm surges.

2. Data

We use hourly still water level observations, tidal predictions, and station datums for 24 tide gauges on the US West Coast from the National Oceanic and Atmospheric Administration (NOAA) Center for Operational Oceanographic Products and Services (CO-OPS). These records are selected because they are relatively long, complete, and span much of the US West Coast (Figure 1; Table S1). They also represent the union of US stations considered either in past studies of ARs and sea level on the US West Coast (Khouakhi and Villarini, 2016; Shinoda et al., 2019) or in government reports on HTFs (e.g., Sweet et al., 2021), allowing us to interpret our results in light of past findings.

We also use the Scripps Institution of Oceanography AR catalog of Gershunov et al. (2017), which is generated by applying an automated AR detection algorithm to 6-hourly integrated water vapor transport (IVT) and integrated water vapor (IWV) from the National Centers for Environmental Prediction/National Center for Atmospheric Research (NCEP/NCAR) Reanalysis 1 (Kalnay et al., 1996). Landfalling ARs are identified by their spatial extent ($\geq$ 1500 km), temporal duration ($\geq$ 18 hours), IVT ($\geq$ 250 kg m^{-1} s^{-1}), and IWV ($\geq$ 15 mm). The landfalling location of an AR satisfying these criteria is defined as the reanalysis grid cell with the maximum IVT along the coast. The catalog includes the time, location, IWT, IVT, and zonal and meridional wind of ARs at their landfalling locations on a 2.5° $\times$ 2.5° grid along the US West Coast (22.5–57.5°N, 105–135°W; Figure 1) from January 1948 to March 2017. To

complement information provided by the Gershunov et al. (2017) catalog, we also consider daily meridional and zonal wind stress, barometric pressure, and precipitation from the NCEP/NCAR Reanalysis 1.

We consider the data between 1 January 1980 and 31 December 2016. The start date is chosen partly based on the tide-gauge records, many of which begin in the late 1970s. By not considering data prior to 1980, we also avoid possible discontinuities in the reanalysis related to the advent of satellite data in the late 1970s. Data processing and methods specific to the analysis of either HTFs or storm surges are described in the next two sections before the respective results are introduced.

3. High-tide floods

We establish relationships between ARs and HTFs on the US West Coast using a peaks-over-threshold approach (cf. Khouakhi and Villarini, 2016). For each tide gauge, we count the number of days when HTFs occur for at least one hour (HTF days). We identify HTFs when still water levels exceed the local minor flood thresholds defined by Sweet et al. (2018), which range between 56–64 cm above local mean higher high water (Table S1). We also count the number of days when an AR passes nearby a tide gauge (AR days). An AR is nearby a tide gauge when it has IVT ≥ 500 kg m^{-1} s^{-1} at its landfalling location in the grid cell whose centroid is closest to the gauge (Figure 1). Note that results are qualitatively insensitive to reasonable alternative definitions of "nearby" (Figure 3a). We also count the number of days when both a HTF occurs and an AR passes nearby the gauge within ± 24 hours of the HTF (HTF-and-AR days). Finally, we count the hypothetical number of days when HTFs would have occurred

from mean sea-level changes and tides alone, absent any surges, by removing the predicted tide from the hourly water level data, low-pass filtering the non-tidal residuals with a 20-day moving median operator, adding back the predicted tide, and identifying days when the flood threshold is exceeded. We run 1,000 bootstrap iterations to estimate uncertainty due to the finite record length of the data (Supporting Information Text S1). We quantify statistical significance by comparing observed values to values determined synthetically through 1,000 simulations of stochastic processes (Supporting Information Text S2).

HTF days and AR days along the US West Coast show clear spatial structure (Figures 2a, 2b). More HTF days and AR days were experienced on the Northwest Coast than the Southwest Coast. For example, San Diego, California experienced 79 ± 17 HTF days and 259 ± 30 AR days during the study period, whereas Neah Bay, Washington witnessed 329 ± 37 HTF days and 760 ± 54 AR days over that same time. All $\pm$ ranges identify 95% confidence intervals based on bootstrapping. The Puget Sound is an exception to the rule: fewer HTF days and AR days occurred at higher-latitude tide gauges in this estuary compared to lower-latitude tide gauges on the open-ocean coasts of Oregon and Washington, suggesting that these estuarine locations are more sheltered from processes driving HTFs and ARs. Central California also deviates from the trend, as fewer HTF days were observed at mid-latitude locations in this region compared to lower-latitude sites in Southern California. The basic patterns of HTF days and AR days found here are consistent with previous studies. For example, Sweet et al. (2021) report that more HTFs happen on the open coasts of Oregon and

Washington than on the California coast or within the Puget Sound (their Appendix 1), while Neiman et al. (2008) find that more AR days occur on the Northwest Coast of North America than on the Southwest Coast. However, past studies do not interrogate possible connections between HTFs and ARs.

To clarify relationships between ARs and HTFs, we compute percentages of HTF days that are AR days and AR days that are HTF days (Figures 2c, 2d, 3a). The percentage of HTF days that are AR days quantifies whether ARs are a necessary condition for HTFs (values $\sim 100\%$ indicate that HTFs only occur during ARs), while the percentage of AR days that are HTF days measures whether ARs are a sufficient condition for HTFs (values $\sim 100\%$ indicate that ARs always lead to HTFs). On average along the coast, $28\% \pm 2.3\%$ of HTF days are AR days, but values are elevated between Monterey and Arena Cove ($48\% \pm 6.9\%$) in Central California, with the highest percentage ($63\% \pm 19\%$) observed at San Francisco (Figures 2c, 3a). Similar findings were obtained using alternative criteria for evaluating if an AR is near a tide gauge (Figure 3a), meaning that these results are robust to these subjective analysis choices. In comparison, the percentage of AR days that are HTF days is lower on average ($5.2\% \pm 0.4\%$), peaking more to the north, with $10\% \pm 1.1\%$ of AR days being HTF days between Port Orford, Oregon and Toke Point, Washington (Figure 2d), suggesting that ARs alone are seldom sufficient to cause HTFs. Nevertheless, at nearly all sites, values in Figures 2c, 2d, 3a are statistically significant ($P < 0.05$), meaning that HTFs and ARs co-occur more often than expected from random chance, and that ARs are important contributors to HTFs.

HTF and AR frequencies also vary across time (Figure 3b). The annual number of HTFs averaged along the US West Coast varies from 0.7 ± 0.7 to 13 ± 5.9 days per year, while the average number of ARs ranges between 7.2 ± 3.1 and 21 ± 6.3 days per year (Figure 3b). HTF days were highest in 1982 (13 ± 5.9 days) and 1997 (12 ± 5.4 days) during strong positive ENSO events. This observation is consistent with past studies identifying a relationship between ENSO and HTF frequency on the US West Coast (Sweet and Park, 2014; Sweet et al., 2021). The Pearson correlation coefficient between interannual variations in HTF and AR days on the US West Coast (0.2 ± 0.2) is not statistically significant ($P > 0.05$). In contrast, the number of HTF days per year is significantly correlated with annual mean sea-level anomaly averaged along the coast (0.7 ± 0.1, $P < 0.01$; Figure 3b). An even higher correlation (0.9 ± 0.1, $P < 0.01$) is found between observed HTF days and hypothetical HTF days expected from tides and mean sea-level changes, such that the latter explains $66 \pm 14\%$ of the variance in the former, suggesting that changes in these extreme sea-level events are governed more by tides and mean sea-level changes than changes in storminess (cf. Marcos et al., 2015; Menéndez and Woodworth, 2010; Ray and Merrifield, 2019; Thompson et al., 2021).

4. Storm surges

We quantify storm surges and their causes during ARs on the US West Coast using a composite analysis (cf. Shinoda et al., 2019). We identify all ARs passing by tide gauges during the study period. For each AR as it passes by a gauge, we isolate the day when maximum IVT takes place and interpret it as when the gauge experiences the strongest effect of the AR. We then take the associated daily storm surge from the tide gauge,

which we calculate from daily-mean still water level by removing the predicted tide, seasonal cycle, and linear trend, and then applying a high-pass filter based on a 20-day moving median operator.

Storm surges during ARs show clear spatial structure (Figures 4a, 4b, 5a). Surges are larger on average at higher latitudes (Figures 4a, 5a). Mean storm surge during an AR grows from 3.1 ± 1.2 cm at Santa Monica, California to 21 ± 3.2 cm at Toke Point, Washington. Deviations from this trend are apparent at locations in the Puget Sound, where mean surge values are lower than expected from latitude alone, which could reflect important estuarine processes distinct from the mechanisms that mediate storm surge along the open-ocean coastline. Storm surge is also more variable at higher latitudes (Figure 4b). For example, the standard deviation of storm surge during ARs is 4.3 ± 0.8 cm at La Jolla, California, 12 ± 1.6 cm at South Beach, Oregon, and 20 ± 5.3 cm at Toke Point, Washington. [Note that, while we use mean and standard deviation as summary statistics, storm surge distributions are not Gaussian (Figure S1).] Such surges are rarely large enough, when superimposed on mean higher high water, to overtop flood thresholds (cf. Table S1; Figure S1). This corroborates the suggestion made in the previous section that ARs alone are seldom sufficient to cause HTFs.

These basic patterns are qualitatively consistent with previous numerical studies of sea level and ARs as well as past observational studies of storm surge in the region. Considering tide-gauge data during 1935–2014, Bromirski et al. (2017) show that the 99th percentile of hourly non-tidal winter residuals increases steadily from 10–15 cm in Southern California to 45–55 cm in Oregon and Washington (their Figure 2c). Serafin et

al. (2017) reveal that the average and spread of observed annual maxima in hourly non-tidal residuals from 11 tide gauges between La Jolla, California and Neah Bay, Washington increase from south to north along the coast (their Figure 1e). Using a high-resolution ocean general circulation model, Shinoda et al. (2019) report that coastal sea level rises during the days leading up to an AR by between $\lesssim 1$ cm off Southern California to $\gtrsim 4$ cm off Oregon and Washington (their Figure 8h). However, these studies do not establish what processes drive storm surge during landfalling ARs.

To attribute observed surges (Figures 4a, 4b), we use contemporaneous daily zonal and meridional wind stress, barometric pressure, and precipitation from NCEP/NCAR Reanalysis 1 at the grid cells closest to the tide gauges. We remove seasonal cycles and linear trends from the reanalysis and apply a 20-day high-pass filter. To quantify how much storm surge can be understood in terms of local wind, pressure, and precipitation anomalies, we consider a simple model that represents surge as a linear superposition of the atmospheric forcing

$$\zeta = \overbrace{\underbrace{a_\pi \pi + b_\pi \mathcal{H}(\pi)}_{\hat{\zeta}_\pi} + \underbrace{a_\tau \tau + b_\tau \mathcal{H}(\tau)}_{\hat{\zeta}_\tau} + \underbrace{a_p p + b_p \mathcal{H}(p)}_{\hat{\zeta}_p} + \underbrace{a_q q + b_q \mathcal{H}(q)}_{\hat{\zeta}_q}}^{\hat{\zeta}} + \epsilon. \tag{1}$$

Here ζ is storm surge, π and τ are zonal and meridional wind stress, respectively, p is barometric pressure, q is precipitation, $\mathcal{H}$ is Hilbert transform, the a's and b's are real constants, and ϵ is a residual. The Hilbert transform rotates each Fourier component of a time series by $\pm 90°$ (Thomson and Emery, 2014). Thus, including Hilbert transforms on the right-hand side of Eq. (1) allows for general phase relationships between the atmospheric forcing and the oceanic response. For clarity, let $\hat{\zeta}_\pi$, $\hat{\zeta}_\tau$, $\hat{\zeta}_p$, and $\hat{\zeta}_q$ identify the modeled ζ responses to π, τ, p, and q forcing, respectively, and $\hat{\zeta}$ the total modeled ζ

response. We use ridge regression to determine the a's and b's at each tide gauge (Supporting Information Text S3), which is preferable to ordinary least squares given possible collinearity between predictors. Results are based on a ridge-parameter value of $\lambda = 0.3$, but similar findings follow from a range of λ values (Figure S2).

Modeled $\hat{\zeta}$ shows skill in explaining ζ observed at tide gauges (Figures 4, 5). The model reproduces the observed structure that surges grow larger and more variable with latitude along the coast (Figure 4). Mean storm surges from the observations ζ and the model $\hat{\zeta}$ overlap within estimated uncertainties everywhere on the California coast (Figure 5a). Along Oregon and Washington, the model can underestimate observed mean storm surge (by as much as 32% on average at Cherry Point, Washington), possibly due to shrinkage related to the ridge regression, reanalysis errors (e.g., due to coarse grid cells that overlap land and sea), or processes absent from the model (Figure 5a). The model also accounts for most of the observed storm-surge variation at all gauges (Figure 5b), explaining between $57 \pm 20\%$ (La Jolla, California) and $87 \pm 3.4\%$ (Point Reyes, California) of the variance in the data.

The model is also informative of the relative influences of π, τ, p, and q forcing on ζ (Figure 5). Primary contributions to ζ are made by p and τ (Figure 5). On average, $\hat{\zeta}_p$ contributions to mean ζ values are nearly spatially uniform along the coast, ranging between 2–5 cm (Figure 5a). In contrast, average $\hat{\zeta}_\tau$ values become larger with latitude, growing from 0.3 ± 0.9 cm at Santa Monica, California to 11 ± 2.3 cm at Toke Point, Washington. In Southern California and within Puget Sound, $\hat{\zeta}_p$ is the more important contributor to ζ variance, but elsewhere $\hat{\zeta}_\tau$ and $\hat{\zeta}_p$ contribute comparably (Figure 5b).

Forcing by q can also make secondary contributions (Figure 5). Mean $\hat{\zeta}_q$ values are distinguishable from zero at most sites, reaching as high as 2.3 ± 0.8 cm in Point Reyes, California and 3.2 ± 2.0 cm in Toke Point, Washington (Figure 5a). In and around San Francisco Bay, and along portions of the Washington coast, $\hat{\zeta}_q$ explains 10–20% of the ζ variance on average (Figure 5b). In contrast, π forcing is largely insignificant (Figure 5). In most places, estimates of ζ variance explained by $\hat{\zeta}_\pi$ overlap with zero (Figure 5b), and mean $\hat{\zeta}_\pi$ values are indistinguishable from zero or small and negative (Figure 5a). Two reasons may together explain our finding that π is not an important contributor. First, τ anomalies, which are mostly alongshore on the US West Coast, are typically stronger than π anomalies, which are mainly onshore, during ARs at gauges (Figure S3). Second, ζ can be more sensitive to an alongshore wind-stress anomaly than to an onshore wind-stress anomaly of equal magnitude (Supporting Information Text S4; Figure S2). More generally, spatial structures apparent in storm-surge contributors (Figure 5) may have partly to do with variations in the orientation or strength of ARs along the coast.

5. Summary and Discussion

Atmospheric rivers (ARs) typically bring heavy rain, strong wind, and low pressure to the coastal zone. We established relationships between ARs and high-tide floods (HTFs), and identified forcing mechanisms responsible for storm surge during ARs on the US West Coast during 1980–2016. ARs and HTFs co-occur more often than expected from random chance, and 10–63% of HTFs coincide with ARs, depending on location (Figures 2, 3). Interannual variations in HTF days and AR days per year are not significantly correlated (Figure 3), meaning that more ARs do not necessarily result

in more HTFs. Instead, there is a significant correlation between observed HTF days per year and the HTF days expected from tides and mean sea-level changes alone (Figure 3). A linear model including local wind, pressure, and precipitation forcing accounts for $\geq 68\%$ of the average magnitude and 57–87% of the variance in magnitude of storm surges during ARs (Figures 4, 5). Meridional wind and barometric pressure make primary contributions to storm surge, but precipitation has a secondary effect in some places (Figure 5).

HTFs arise from a subtle interplay of distinct processes acting on different timescales. Fewer HTFs would occur from tides and mean sea-level changes in the absence of surges due to ARs and other events (Figure 3). However, surges associated with ARs are rarely large enough, when added to mean higher high water, to cause HTFs on their own (Figure 3). It is only when superimposed on a favorable tide or mean sea-level anomaly that storm surges related to ARs are generally capable of exceeding HTF thresholds. For a full understanding of observed HTFs, the effects of surges, tides, and mean sea level must all be considered.

This paper advances knowledge of hazards related to ARs and the oceanic response to atmospheric forcing on the US West Coast. Past studies emphasize hydrological impacts of ARs related to extreme precipitation (Payne et al., 2020), but we show that ARs also drive coastal impacts related to sea level. By quantifying relationships between HTFs and ARs, and identifying the factors driving storm surge during these events, we resolve outstanding questions in the literature (Bromirski et al., 2017; Khouakhi and Villarini, 2016; Shinoda et al., 2019). This paper elucidates a mechanism of HTFs, occurrences of

which are increasing on much of the US Coast (Sweet et al., 2021), and will accelerate into the future (Thompson et al., 2021). Our work is consistent with the notion that observed changes in sea-level extremes are attributable more to changes in mean sea level and the tides than to changes in storminess (Marcos et al., 2015; Menéndez and Woodworth, 2010; Ray and Merrifield, 2019; Thompson et al., 2021). Our results also underscore the importance of understanding locally forced high-frequency sea-level variability on the US West Coast (Battisti and Hickey, 1984; Bromirski et al., 2017; Chapman, 1987; Gill and Clarke, 1974; Ryan and Noble, 2006; Verdy et al., 2014).

We conclude with some limitations of our study and future research directions.

1. Space constraints precluded a complete study of the spatiotemporal statistics of HTFs and ARs on the US West Coast. Future studies should consider more granular details, such as temporal variation in HTF and AR co-occurrences at individual tide gauges across various timescales, including the seasonal cycle and decadal trends, to identify whether sea-level rise influences the covariance between HTFs and ARs, and if HTFs due to ARs occur mainly in particular months of the year (Thompson et al., 2021).

2. We focused on the US West Coast, but ARs make landfall in other mid- and high-latitude regions (Payne et al., 2020). Links should be established between ARs and sea-level extremes on a more global basis (cf. Ridder et al., 2018; Carvajal et al., 2021).

3. We used the AR catalog of Gershunov et al. (2017) and NCEP/NCAR Reanalysis 1 (Kalnay et al., 1996). However, other AR catalogues have been published, which can differ in terms of their detection algorithms (Rutz et al., 2019; Shields et al., 2018), and other reanalysis products are available, which can feature different spacetime resolutions,

data constraints, and assimilation methods (Gelaro et al., 2017; Hersbach et al., 2020; Kobayashi et al., 2015). Multiple catalogs and reanalyses should be considered to more thoroughly quantify uncertainty.

4. We focused on storm surge and HTFs, but ARs could affect other quantities of interest to coastal impacts, such as waves and erosion (Serafin et al., 2017; Theuerkauf et al., 2014). A more comprehensive assessment of coastal hazards due to landfalling ARs, including their role in compound events (AghaKouchak et al., 2020), should be made.

5. We used flood thresholds from the common impact threshold framework of Sweet et al. (2018), which is a consistent national coastal flood metric, applicable everywhere tidal datums are established. However, flood thresholds based on this framework may be lower or higher than levels that correspond to local impacts (Kriebel and Geiman, 2013). The sensitivity of our results to other definitions of flood threshold should be quantified.

6. Our investigation of storm surge was statistical in nature. Regression coefficients found empirically from the data are consistent with basic expectations for a coastal-trapped barotropic sea-level response to local wind, pressure, and precipitation forcing over a frictional shelf (Supporting Information Text S4; Figure S2), suggesting that we identify causal relationships between storm surge and atmospheric forcing. Even so, a more physics-based assessment would be informative, allowing the relative roles of the various (correlated) forcing mechanisms to be more unambiguously identified. Because precipitation is not often identified as a driver of storm surge (Gill, 1982; Pugh and Woodworth, 2014), it would be particularly informative to test our hypothesis that precipitation can contribute to storm surge during ARs.

7. We used observations of the past four decades, but the nature of ARs could change under future warming. While their dynamical response to climate change remains uncertain (Shepherd et al., 2014; Vallis et al., 2015), ARs are expected to become more frequent (Espinoza et al., 2018), contain more moisture (Dettinger, 2011), and shift poleward (Yin, 2005) as the climate changes. It remains to evaluate how future changes in ARs would aggravate coastal impacts already expected from future sea-level rise (Jevrejeva et al., 2019; Kopp et al., 2017).

Acknowledgments. This work was supported by National Aeronautics and Space Administration Sea Level Change Team awards 80NSSC20K1241 and 80NM0018D0004 (to C. G. P.). The contribution from F. W. L. and J. T. R. represents research carried out at the Jet Propulsion Laboratory, California Institute of Technology, under a contract with the National Aeronautics and Space Administration (80NM0018D0004).

Data Availability Statement. Tide-gauge data, tidal predictions, and station datum information are from the NOAA Tides and Currents Service (`https://tidesandcurrents.noaa.gov/`). Reanalysis fields are from the NOAA Physical Sciences Laboratory (`https://psl.noaa.gov/data/gridded/data.ncep.reanalysis.html`). The AR data are from the Scripps Institution of Oceanography (`https://weclima.ucsd.edu/data-products/`). Codes used to analyze the data are available through Zenodo (`https://zenodo.org/record/5247207`).

References

AghaKouchak, A., Chiang, F., Huning, L. S., Love, C. A., Mallakpour, I., Mazdiyasni, O., Moftakhari, H., Papalexiou, S. M., Ragno, E., & Sadegh, M. (2020). Climate Extremes and Compound Hazards in a Warming World. *Annual Review of Earth and Planetary Sciences*, *48*, 519–548.

Battisti, D. S., & Hickey, B. M. (1984). Application of Remote Wind-Forced Coastal Trapped Wave Theory to the Oregon and Washington Coasts. *Journal of Physical Oceanography*, *14*, 887–903.

Bromirski, P. D., Flick, R. E., & Miller, A. J. (2017). Storm surge along the Pacific coast of North America. *Journal of Geophysical Research: Oceans*, *122*, 441–457.

Carvajal, M., Winckler, P., Garreaud, R., Igualt, F., Contreras-López, M., Averil, P., Cisternas, M., Gubler, A., & Breuer, W. A. (2021). Extreme sea levels at Rapa Nui (Easter Island) during intense atmospheric rivers. *Natural Hazards*, *106*, 1619–1637.

Chapman, D. C. (1987). Application of Wind-Forced, Long, Coastal-Trapped Wave Theory Along the California Coast. *Journal of Geophysical Research*, *92*, C2, 1798–1816.

Cordeira, J. M., Ralph, F. M., & Moore, B. J. (2013). The development and evolution of two atmospheric rivers in proximity to western North Pacific tropical cyclones in October 2010. *Monthly Weather Review*, *141*, 2434–4255.

Dettinger, M. D. (2013). Atmospheric rivers as drought busters on the US West Coast. *Journal of Hydrometeorology*, *14*, 1721–1732.

Dettinger, M. D. (2011). Climate change, atmospheric rivers, and floods in California—a multimodel analysis of storm frequency and magnitude changes. *Journal of the American Water Resources Association*, *14*, 514–523.

Du, X., Hendy, I., & Schimmelmann, A. (2018). A 9000-year flood history for Southern California: a revised stratigraphy of varved sediments in Santa Barbara Basin. *Marine Geology*, *397*, 29–42.

Espinoza, V., Waliser, D. E., Guan, B., Lavers, D. A., & Ralph, F. M. (2018). Global analysis of climate change projection effects on atmospheric rivers. *Geophysical Research Letters*, *45*, 4299–4308.

Gelaro, R., McCarty, W., Suárez, M. J., Todling, R., Molod, A., Takacs, L., Randles, C. A., Darmenov, A., Bosilovich, M. G., Reichle, R., Wargan, K., Coy, L., Cullather, R., Draper, C., Akella, S., Buchard, V., Conaty, A., da Silva, A. M., Gu, W., Kim, G.-K., Koster, R., Lucchesi, R., Merkova, D., Nielsen, J. E., Partyka, Pawson, S., Putman, W., Rienecker, M., Schubert, S. D., Sienkiewicz, M., & Zhao, B. (2017). The Modern-Era Retrospective Analysis for Research and Applications, Version 2 (MERRA-2). *Journal of Climate*, *30*, 14, 5419–5454.

Gershunov, A., Shulgina, T., Ralph, F. M., Lavers, D. A., & Rutz, J. J. (2017). Assessing the climate-scale variability of atmospheric rivers affecting western North America. *Geophysical Research Letters*, *44*, 7900–7908.

Gill, A. E. (1982). Atmosphere-Ocean Dynamics. Academic Press, San Diego, 662 pp.

Gill, A. E., & Clarke, A. J. (1974). Wind-induced upwelling, coastal currents, and sea-level changes. *Deep-Sea Research*, *21*, 325–345.

Hendy, I. L., Napier, T. J., & Schimmelmann, A. (2015). From extreme rainfall to drought: 250 years of annually resolved sediment deposition in Santa Barbara Basin, California. *Quaternary International*, *387*, 3?12 (2015).

Hersbach, H., Bell, B., Berrisford, P., Hirahara, S., Hor/'anyi, A., Muñoz-Sabater, J., Nicolas, J., Peubey, C., Radu, R., Schepers, D., Simmons, A., Soci, C., Abdalla, S., Abellan, X., Balsamo, G., Bechtold, P., Biavati, G., BIdlot, J., Bonavita, M., De Chiara, G., Dahlgren, P., Dee, D., Diamantakis, M., Dragani, R., Flemming, J., Forbes, R., Fuentes, M., Geer, A., Haimberger, L., Healy, S., Hogan, R. J., Hólm, E., Janisková, M., Keeley, S., Laloyaux, P., Lopez, P., Lupu, C., Radnoti, G., de Rosnay, P., Rozum, I., Vamborg, F., Villaume, S., & Thépaut, J.-N. (2020). The ERA5 global reanalysis. *Quarterly Journal of the Royal Meteorological Society*, *146*, 730, 1999–2049.

Hino, M., Belanger, S. T., Field, C. B., Davis, A. R., & Mach, K. J. (2019). High-tide flooding disrupts local economic activity. *Science Advances*, *5*, eaau2736.

Jevrejeva, S., Frederikse, T., Kopp, R. E., Le Cozannet, G., Jackson, L. P., & van de Wal, R. S. W. (2019). Probabilistic Sea Level Projections at the Coast by 2100. *Surveys in Geophysics*, *40*, 1673–1696.

Kalnay, E., Kanamitsu, M., Kistler, R., Collins, W., Deaven, D., Gandin, L., Iredell, M., Saha, S., White, G., Woollen, J., Zhu, Y., Chelliah, M., Ebisuzaki, W., Higgins, W., Janowiak, J., Mo, K. C., Ropelewski, C., Wang, J., Leetmaa, A., Reynolds, R. Jenne, R., & Joseph, D. (1996). The NCEP/NCAR 40-year reanalysis project. *Bulletin of the American Meteorological Society*, *77*, 3, 437–471.

435 Khouakhi, A., & Villarini, G. (2016). On the relationship between atmospheric rivers
436 and high sea water levels along the US West Coast. *Geophysical Research Letters*, *43*,
437 8815–8822.

438 Kobayashi, S., Ota, Y., Harada, Y., Ebita, A., Moriya, M., Onoda, H., Onogi, K.,
439 Kamahori, H., Kobayashi, C., Endo, H., Miyaoka, K., & Takahashi, K. (2015). The
440 JRA-55 Reanalysis: General Specifications and Basic Characteristics. *Journal of the*
441 *Meteorological Society of Japan*, *93*, 1, 5–48.

442 Kriebel, D. L., & Geiman, J. D. (2013). A Coastal Flood Stage to Define Existing and
443 Future Sea-Level Hazards. *Journal of Coastal Research*, *30*, 5, 1017–1024.

444 Kopp, R. E., DeConto, R. M., Bader, D. A., Hay, C. C., Horton, R. M., Kulp, S.,
445 Oppenheimer, M., Pollard, M., & Strauss, B. H. (2017). Evolving Understanding of
446 Antarctic Ice-Sheet Physics and Ambiguity in Probabilistic Sea-Level Projections.
447 *Earth's Future*, *5*, 1217–1233.

448 Marcos, M., Calafat, F. M., Berihuete, A., & Dangendorf, S. (2015). Long-term
449 variations in global sea level extremes. *Journal of Geophysical Research: Oceans*, *120*,
450 8115–8134.

451 Menéndez, M., & Woodworth, P. L. (2010). Changes in extreme high water levels base
452 don a quasi-global tide-gauge data set. *Journal of Geophysical Research*, *115*, C1001.

453 Moftakhari, H. R., AghaKouchak, A., Sanders, B. F., & Matthew, R. A. (2017).
454 Cumulative hazard: The case of nuisance flooding. *Earth's Future*, *5*, 214–223.

455 Moftakhari, H. R., AghaKouchak, A., Sanders, B. F., Allaire, M., & Matthew, R. A.
456 (2018). What Is Nuisance Flooding? Defining and Monitoring an Emerging Challenge.

457 *Water Resources Research*, *54*, 4218–4227.

458 Neiman, P. J., Ralph, F. M., Wick, G. A., Lundquist, J. D., & Dettinger, M. D. (2008).
459 Meteorological characteristics and overland precipitation impacts of atmospheric rivers
460 affecting the West Coast of North America based on eight years of SSM/I satellite
461 observations. *Journal of Hydrometeorology*, *9*, 22–47.

462 Newman, M., Kiladis, G. N., Weickmann, K. M., Ralph, F. M., & Sardeshmukh, P. D.
463 (2012). Relative contributions of synoptic and low-frequency eddies to time-mean
464 atmospheric moisture transport, including the role of atmospheric rivers. *Journal of*
465 *Climate*, *25*, 7341–7361.

466 Oakley, N. S., Lancaster, J. T., Kaplan, M. L., & Ralph, F. M. Synoptic conditions
467 associated with cool season post-fire debris flows in the Transverse Ranges of southern
468 California. *Natural Hazards*, *88*, 327–354.

469 Oakley, N. S., Lancaster, J. T., Hatchett, B. J., Stock, J., Ralph, F. M., Roj, S., &
470 Lukashov, S. (2018). A 22-year climatology of cool season hourly precipitation
471 thresholds conducive to shallow landslides in California. *Earth Interactions*, *22*, 1–35.

472 Payne, A. E., Demory, M.-E., Leung, L. R., Ramos, A. M., Shields, C. A., Rutz, J. J.,
473 Siler, N., Villarini, G., Hall, A., & Ralph, F. M. (2020). Responses and impacts of
474 atmospheric rivers to climate change. *Nature Reviews Earth and Environment*, *1*,
475 143–157.

476 Pugh, D., & Woodworth, P. (2014). Sea-Level Science: Understanding Tides, Surges,
477 Tsunamis, and Mean Sea-Level Changes. Cambridge University Press, Cambridge, 407
478 pp.

Ralph, F. M., Neiman, P. J., & Wick, G. A. (2004). Satellite and CALJET aircraft observations of atmospheric rivers over the eastern North Pacific Ocean during the winter of 1997/98. *Monthly Weather Review*, *132*, 1721–1745.

Ralph, F. M., Coleman, T. A., Neiman, P. J., Zamora, R. J., & Dettinger, M. D. (2013) Observed impacts of duration and seasonality of atmospheric river landfalls on soil moisture and runoff in coastal Northern California. *Journal of Hydrometeorology*, *14*, 443–459.

Ralph, F. M., Iacobellis, S. F., Neiman, P. J., Cordeira, J. M., Spackman, J. R., Waliser, D. E., Wick, G. A., White, A. B., & Fairall, C. (2017). Dropsonde observations of total integrated water vapor transport within North Pacific atmospheric rivers. *Journal of Hydrometeorology*, *18*, 2577–2596.

Ray, R. D., & Merrifield, M. A. (2019). The Semiannual and 4.4-Year Modulations of Extreme High Tides. *Journal of Geophysical Research: Oceans*, *124*, 5907–5922.

Ridder, N., de Vries, H., & Drijfhout, S. (2018). The role of atmospheric rivers in compound events consisting of heavy precipitation and high storm surges along the Dutch coast. *Natural Hazards and Earth System Sciences*, *18*, 3311–3326.

Rutz, J. J., Shields, C. A., Lora, J. M., Payne, A. E., Guan, B., Ullrich, P., O'Brien, T., Leung, L. R., Ralph, F. M., Wehner, M., Brands, S., Collow, A., Goldenson, N., Gorodetskaya, I., Griffith, H., Kashinath, K., Kawzenuk, B., Krishnan, H., Kurlin, V., Lavers, D., Magnusdottir, G., Mahoney, K., McClenny, E., Muszynski, G., Nguyen, P. D., Prabhat, M., Qian, Y., Ramos, A. M., Sarangi, C., Sellars, S., Shulgina, T., Tome, R., Waliser, D., Walton, D., Wick, G., Wilson, A. M., & Viale, M. (2019). The

atmospheric river tracking method intercomparison project (ARTMIP): quantifying uncertainties in atmospheric river climatology. *Journal of Geophysical Research: Atmospheres*, *124*, 13777–13802.

Ryan, H. F., & Noble, M. A. (2006). Alongshore Wind Forcing of Coastal Sea Level as a Function of Frequency. *Journal of Physical Oceanography*, *36*, 2173–2184.

Serafin, K. A., Ruggiero, P. & Stockdon, H. F. (2017). The relative contributions of waves, tides, and nontidal residuals to extreme total water levels on U.S. West Coast sandy beaches. *Geophysical Research Letters*, *44*, 1839–1847.

Shepherd, T. G. (2014). Atmospheric circulation as a source of uncertainty in climate change projections. *Nature Geoscience*, *7*, 703–708.

Shields, C. A., Rutz, J. J., Leung, L-Y., Ralph, F. M., Wehner, M., Kawzenuk, B., Lora, J. M., McClenny, E., Osborne, T., Payne, A. E., Ullrich, P., Gershunov, A., Goldenson, N., Guan, B., Qian, Y., Ramos, A. M., Sarangi, C., Sellars, S., Gorodetskaya, I., Kashinath, K., Kurlin, V., Mahoney, K., Muszynski, G., Pierce, R., Subramanian, A. C., Tome, R., Waliser, D., Walton, D., Wick, G., Wilson, A., Lavers, D., Prabhat, M., Collow, A., Krishnan, H., Magnusdottir, G., & Nguyuen, P. (2018). Atmospheric river tracking method intercomparison project (ARTMIP): project goals and experimental design. *Geoscientific Model Development*, *11*, 2455–2474.

Shinoda, T., Zamudio, L., Guo, Y., Metzger, E. J., & Fairall, C. W. (2019). Ocean variability and air-sea fluxes produced by atmospheric rivers. *Scientific Reports*, *9*, 2152.

Sweet, W. V., & Park, J. (2014). From the extreme to the mean: Acceleration and tipping points of coastal inundation from sea level rise. *Earth's Future*, *2*, 579–600.

Sweet, W. V., Dusek, G., Obeysekera, O., & Marra, J. (2018). Patterns and Projections of High Tide Flooding Along the U.S. Coastline Using a Common Impact Threshold. NOAA Technical Report NOS CO-OPS 086, 56 pp.

Sweet, W. V., Simon, S. Dusek, G., Marcy, D., Brooks, W., Pendleton, M., & Marra, J. (2021). 2021 State of High Tide Flooding and Annual Outlook. National Oceanic and Atmospheric Administration, 28 pp.

Theuerkauf, E. J., Rodriguez, A. B., Fegley, S. R., & Luettich, R. A. (2014). Sea level anomalies exacerbate beach erosion. *Geophysical Research Letters*, *41*, 5139–5147.

Thomson, R. E., & Emery, W. J. (2014). Data Analysis Methods in Physical Oceanography, Third Edition. Elsevier, Waltham, 716 pp.

Thompson, P. R., Widlansky, M. J., Hamlington, B. D., Merrifield, M. A., Marra, J. J. Mitchum, G. T., & Sweet, W. (2021). Rapid increases and extreme months in projections of United States high-tide flooding. *Nature Climate Change*, *11*, 584–590.

Vallis, G. K., Zurita-Gotor, P., Cairns, C., & Kidston, J. (2015). Response of the large-scale structure of the atmosphere to global warming. *Quarterly Journal of the Royal Meteorological Society*, *141*, 1479–1501.

Verdy, A., Mazloff, M. R., Cornuelle, B. D., & Kim, S. Y. (2014). Wind-Driven Sea Level Variability on the California Coast: An Adjoint Sensitivity Analysis. *Journal of Physical Oceanography*, *44*, 297–318.

Wang, S. Y. S., Yoon, J.-H., Becker, E., & Gillies, R. (2017). California from drought to deluge. *Nature Climate Change*, *7*, 465–468.

White, A. B., Moore, B. J., Gottas, D. J., & Neiman, P. J. (2019). Winter storm conditions leading to excessive runoff above California?s Oroville Dam during January and February 2017. *Bulletin of the American Meteorological Society*, *100*, 55–70.

Yin, J. H. (2005). A consistent poleward shift of the storm tracks in simulations of 21st century climate. *Geophysical Research Letters*, *32*, L18701.

Zhu, Y., & Newell, R. E. (1998). A proposed algorithm for moisture fluxes from atmospheric rivers. *Monthly Weather Review*, *126*, 725–735.

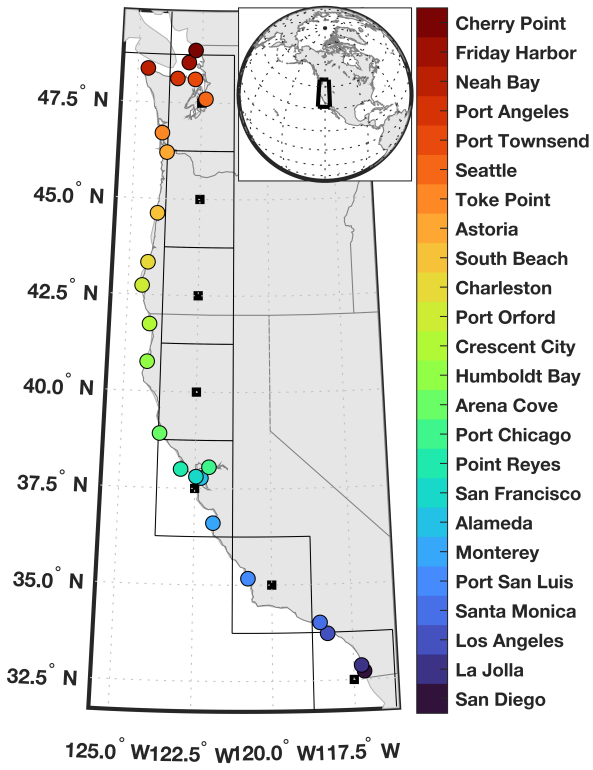

552 **Figure 1.** Study region. Colored circles identify locations of tide gauges. Thick black squares
553 mark centers of grid cells in the catalog of ARs. Thin square outlines denote $2.5° \times 2.5°$ catalog
554 grid-cell boundaries. Inset shows study region in global context.

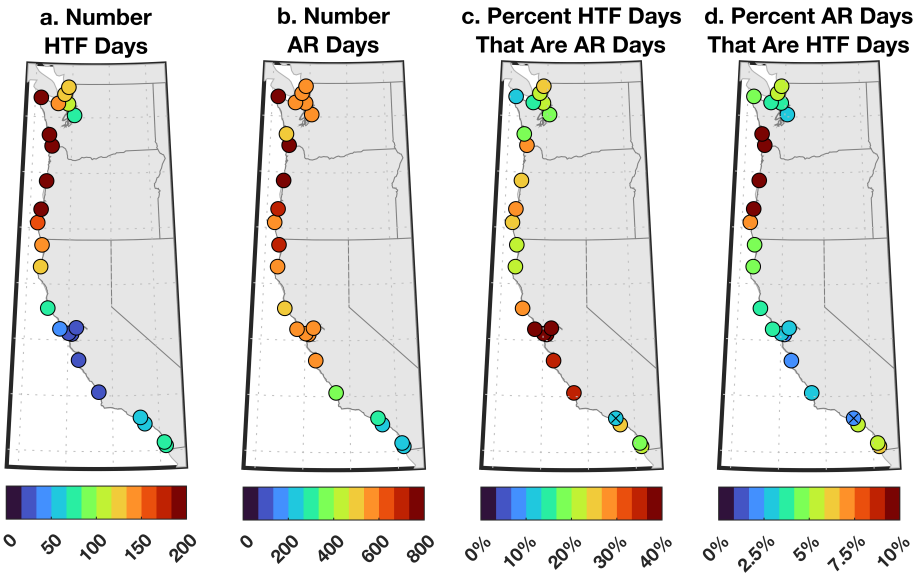

Figure 2. Number of **(a.)** HTF days and **(b.)** AR days at tide gauges during 1980–2016. Percentage of **(c.)** HTF days experiencing ARs, and **(d.)** AR days experiencing HTFs. The "x" at Santa Monica, California in panels (c.) and (d.) indicates that the value is not significant given the null hypothesis of two uncorrelated stochastic Poisson processes (Supporting Information Text S2).

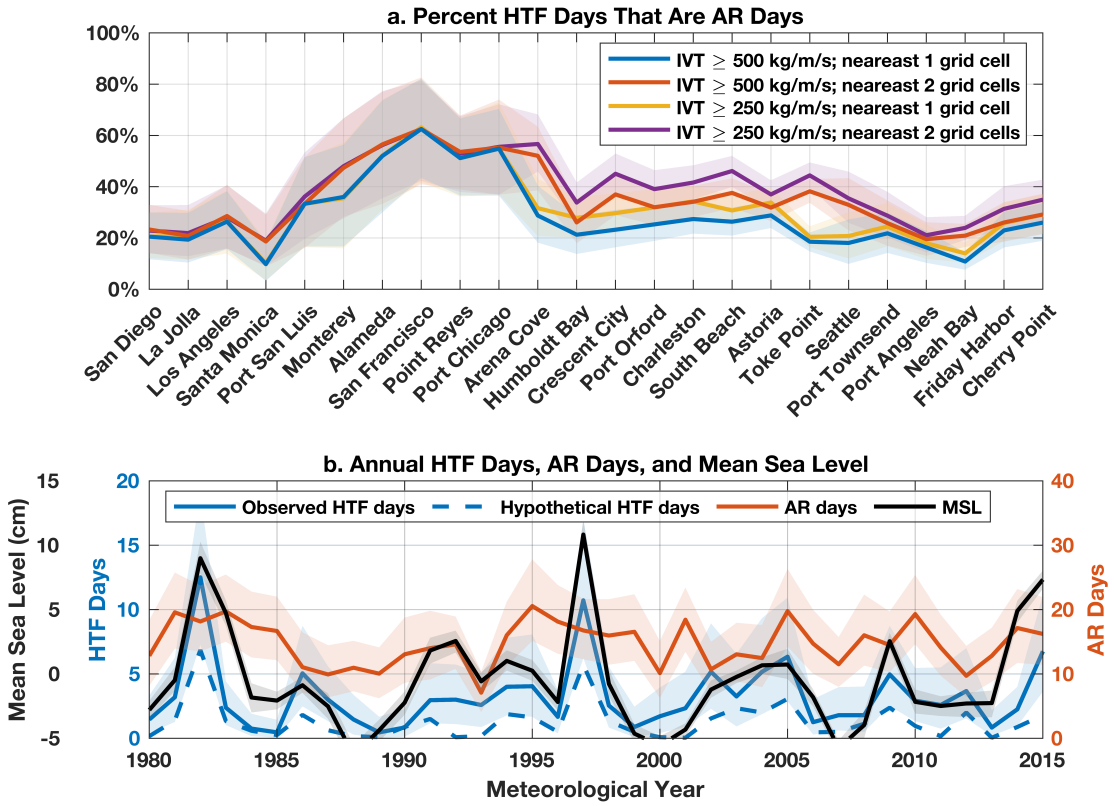

Figure 3. (a.) Percentage of HTF days with ARs during 1980–2016. Different colors identify different criteria applied to determine whether an AR is nearby during a HTF (i.e., whether the minimum IVT threshold is 250 or 500 kg m^{-1} s^{-1} and 1 or 2 nearby grid cells are considered). **(b.)** Averages across all tide gauges along the US West Coast of yearly observed HTF days (blue), AR days (orange), and annual mean sea level (black). Thick lines and shaded values are, respectively, bootstrap estimates of average values and 95% confidence intervals. Blue dashed line is the best estimate of the number of HTF days per year expected hypothetically from tides and mean sea-level changes (see text for details). Note that the horizontal axis has units of meteorological years (April–May).

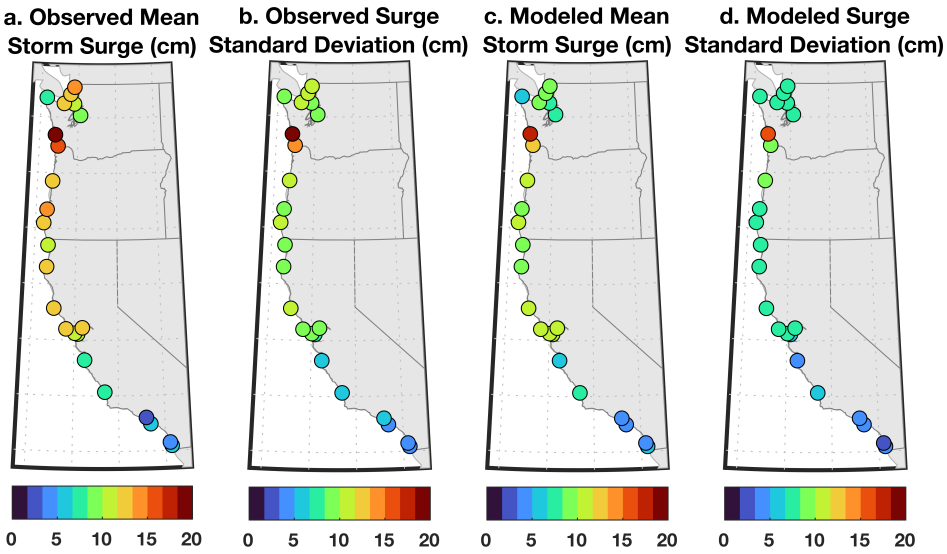

Figure 4. Composite **(a.)** averages and **(b.)** standard deviations of storm surge during ARs observed by tide gauges over 1980–2016. **(c.), (d.)** As in (a.), (b.) but based on the ridge-regression model including local wind, pressure, and precipitation forcing.

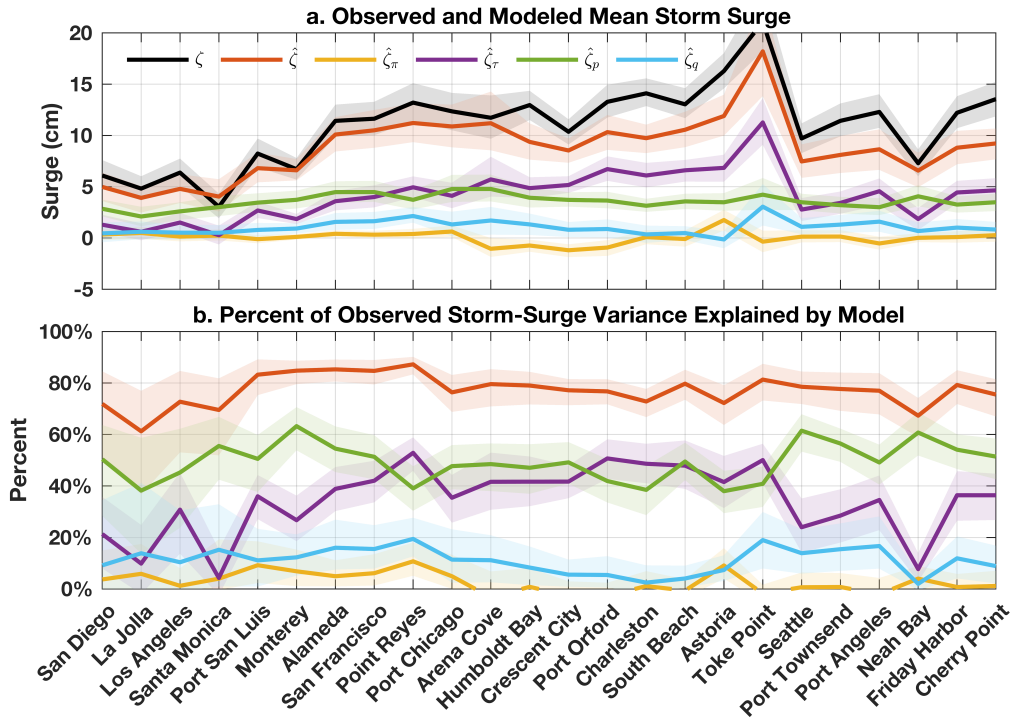

Figure 5. (a.) Average ζ value across all ARs observed by tide gauges during 1980–2016 (black) alongside corresponding total $\hat{\zeta}$ (orange), zonal-wind-driven $\hat{\zeta}_\pi$ (yellow), meridional-wind-driven $\hat{\zeta}_\tau$ (purple), pressure-driven $\hat{\zeta}_p$ (green), precipitation-driven $\hat{\zeta}_q$ (blue) modeled values. **(b.)** Observed ζ variance explained by the various model estimates at each tide gauge during 1980–2016. Thick lines and shaded values are, respectively, bootstrap estimates of the mean and 95% confidence interval. We define the variance V in a variable x explained by another variable y as $V = 100\% \times \left[1 - \mathrm{var}\left(x - y\right) / \mathrm{var}\left(x\right)\right]$ where var is the variance operator.

Supporting Information for "High-Tide Floods and Storm Surges During Atmospheric Rivers on the US West Coast"

Christopher G. Piecuch[1], Sloan Coats[2], Sönke Dangendorf[3], Felix W. Landerer[4], J. T. Reager[4], Philip R. Thompson[2], and Thomas Wahl[5]

Christopher G. Piecuch, Woods Hole Oceanographic Institution, 266 Woods Hole Road, Woods Hole, MA 02543, USA. (cpiecuch@whoi.edu)

[1]Woods Hole Oceanographic Institution, Woods Hole, MA, USA.

[2]University of Hawai'i at Mānoa, Honolulu, HI, USA.

[3]Old Dominion University, Norfolk, VA, USA

[4]Jet Propulsion Laboratory, California Institute of Technology, Pasadena, CA, USA.

[5]University of Central Florida, Orlando, FL, USA.

S1. Bootstrapping

We use bootstrapping to quantify uncertainty related to the finite record lengths of the data (e.g., Efron and Hastie, 2016). Given time-series data (e.g., hourly tide-gauge water-level observations), for each sample statistic (e.g., mean, standard deviation), we perform 1,000 iterations of randomly selecting (with replacement) a number of data values equal to the length of the original data record and computing the sample statistic. Since values can be repeated or omitted, statistics computed during any given iteration can differ from the value computed from the original data. Values in the main text are usually given in the form of averages or 95% confidence intervals from the resulting distributions.

Note that, for quantities that depend on the covariance between time series (e.g., variance explained, co-occurrence of HTFs and ARs), we randomly select the time points at each bootstrapping iteration and use those common time points for each data series involved in the calculation. For example, we compute regression coefficients using contemporaneous storm surge, wind stress, barometric pressure, and freshwater flux.

A caveat of the bootstrapping method used here is that it is performed independently at each tide-gauge location. Thus, when computing spatial averages, we will tend to underestimate the true uncertainties, since the approach effectively assumes that errors are uncorrelated across tide gauges. In reality, there are spatial dependencies in the processes under consideration that should be taken into account in a more complete future spatiotemporal statistical analysis.

S2. Hypothesis testing

To evaluate whether relationships between quantities of interest in section 3 of the main text are statistically significant, we run Monte Carlo simulations of synthetic stochastic processes. For example, we compute the significance of the co-occurrence of (or correlation between) HTFs and ARs by comparing observed values (Figures 2, 3) to values expected from two independent stochastic daily Poisson processes with parameter values determined from the observed numbers of HTF days and AR days during the study period. The corresponding P-value is calculated as the fraction of the time that co-occurrences are more frequent (or that correlations are stronger) in the simulations than in the observations. Likewise, we quantify the significance of the correlation between interannual time series of HTFs and mean sea level (Figure 3b) by comparing to simulated correlations between a random Poisson process with parameter value based on the observed number of HTFs and a random zero-mean Gaussian process with variance parameter equal to the variance of the observed mean sea-level time series.

S3. Ridge regression

Consider the linear model

$$\mathbf{y} = \mathbf{X}\beta + \epsilon \tag{S1}$$

where $\mathbf{y}$ is the $n \times 1$ known observational vector, $\mathbf{X}$ is the $n \times p$ known structure matrix, ϵ is the $n \times 1$ noise vector, and β is the $p \times 1$ vector of unknown parameters to be determined. With reference to Eq. (1) in the main text, the vector $\mathbf{y}$ in Eq. (S1) corresponds to the observed storm surge, matrix $\mathbf{X}$ corresponds to the local wind, pressure, and precipitation forcing, and vector β corresponds to the a and b terms.

The ordinary least squares estimate of the parameter vector is

$$\hat{\beta}_{\mathrm{OLS}} = \left(\mathbf{X}^{\mathsf{T}}\mathbf{X}\right)^{-1}\mathbf{X}^{\mathsf{T}}\mathbf{y}. \tag{S2}$$

If elements of the structure matrix are collinear, then the inner product matrix $\mathbf{X}^{\mathsf{T}}\mathbf{X}$ can be poorly conditioned (or even singular), resulting in large uncertainties on $\hat{\beta}_{\mathrm{OLS}}$. This is a concern in the present context, since the predictor variables can be correlated. As just one randomly selected example, the Pearson correlation coefficient between anomalous meridional wind stress and barometric pressure across 108 landfalling ARs at Port Chicago, California during 1980–2016 is -0.53 ($P < 0.01$).

Ridge regression is a regularization technique that gives more accurate (but biased) estimates relative to ordinary least squares in problems with correlated predictors. The ridge-regression estimate of the parameter vector is (e.g., Efron and Hastie, 2016)

$$\hat{\beta}_{\mathrm{RR}} = \left(\mathbf{X}^{\mathsf{T}}\mathbf{X} + \lambda\mathsf{I}\right)^{-1}\mathbf{X}^{\mathsf{T}}\mathbf{y}. \tag{S3}$$

where $\lambda > 0$ is a real constant and I is the identity matrix. See Efron and Hastie (2016) for a Bayesian interpretation of λ in terms of prior belief.

We use Eq. (S3) with $\lambda = 0.3$ to solve for the a's and b's in Eq. (1) in the main text. Results are robust to the selection of λ, and similar regression coefficients are found for a wide range of λ values (Figure S2). Before evaluating Eq. (S3), we standardize the predictors to have zero mean and unit sum of squares. We also remove the mean from the observational vector. After computing $\hat{\beta}_{\mathrm{RR}}$, we rescale the regression coefficients back to their respective physical units (cf. Figure S2).

S4. Theoretical coefficients

To interpret regression coefficients determined empirically from the data (Figure S2), we build a model of the coastal sea-level response to surface wind, pressure, and precipitation forcing. Imagine a straight coastline extending infinitely in the meridional/alongshore (y) coordinate. The coast faces the ocean to the west, with the origin in the zonal/onshore coordinate (x) at the coast. Offshore positions have values $x < 0$. We consider the following form of shallow water equations

$$\eta_t + H u_x = 0, \tag{S4}$$

$$-fv = -g\left[\eta + \frac{1}{\rho g} p + \int^t q(t')\ dt'\right]_x + \frac{1}{\rho H}\pi, \tag{S5}$$

$$v_t + fu = \frac{1}{\rho H}\tau - \gamma v. \tag{S6}$$

Here t is time, subscript is partial differentiation, p is barometric pressure, q is precipitation, π and τ are onshore and alongshore wind stress, respectively, η is adjusted sea level (Gill, 1982; Ponte, 2006)

$$\eta \doteq \zeta - \int^t q(t')\ dt', \tag{S7}$$

where ζ is sea level, u is onshore velocity, v is alongshore velocity, ρ is constant ocean density, g is gravitational acceleration, f is the Coriolis parameter, H is constant ocean depth, and $\gamma \doteq r/H$ is an inverse timescale, where r is a linear friction coefficient.

The choice of the locally forced form of Eqs. (S4)–(S6) is partly motivated by the regression analysis, which suggests that observed storm surges can be largely understood in terms of local wind, pressure, and precipitation forcing (Figure 5). We have omitted terms involving the onshore velocity in the onshore momentum equation, and the effects

of stratification, nonlinearities, and alongshore dependence in the governing equations. These omissions follow formally from the assumptions that Burger and Rossby numbers are small, alongshore scales are much larger than onshore scales, alongshore motions are much stronger than onshore motions, and frequencies are sub-inertial.

We suppose that surface forcing by an AR is described by temporal plane waves that decay spatially away from the coast

$$F\left(x,t\right)=F_{0}\exp\left(kx-i\sigma t\right),\ F\in\left\{p,q,\pi,\tau\right\}, \tag{S8}$$

where $i\doteq\sqrt{-1}$, σ is angular frequency, and k and F_0 are real constants. We demand that the oceanic response is separable and described by plane waves in time

$$y\left(x,t\right)=\tilde{y}\left(x\right)\exp\left(-i\sigma t\right),\ y\in\left\{\eta,u,v\right\}, \tag{S9}$$

where $\tilde{\eta}$, $\tilde{u}$, and $\tilde{v}$ are functions of the onshore coordinate to be determined.

Inserting (S8) and (S9) into (S4)–(S6) and rearranging gives a second-order inhomogeneous linear ordinary differential equation for onshore structure

$$\tilde{\eta}_{xx}-\kappa^{2}\tilde{\eta}=\left[-\frac{k}{\rho g}p_{0}-i\frac{k}{\sigma}q_{0}+\frac{1}{\rho gH}\pi_{0}+\frac{f}{\rho gH}\left(\frac{\gamma+i\sigma}{\gamma^{2}+\sigma^{2}}\right)\tau_{0}\right]k\exp\left(kx\right) \tag{S10}$$

where $\kappa\doteq s\exp\left(i\varphi\right)/L_{R}$ is complex, with barotropic Rossby radius of deformation $L_{R}\doteq\sqrt{gH}/f$, amplitude $s\doteq\left[1+\left(\gamma/\sigma\right)^{2}\right]^{-1/4}$, and phase $\varphi\doteq\frac{1}{2}\arctan\left(-\gamma/\sigma\right)$.

The boundary conditions are

$$\eta\rightarrow0\text{ as }x\rightarrow-\infty, \tag{S11}$$

$$\tilde{\eta}_{x}=-\frac{k}{\rho g}p_{0}-i\frac{k}{\sigma}q_{0}+\frac{1}{\rho gH}\pi_{0}+\frac{f}{\rho gH}\left(\frac{\gamma+i\sigma}{\gamma^{2}+\sigma^{2}}\right)\tau_{0}\text{ at }x=0. \tag{S12}$$

The first boundary condition demands a shore-trapped solution, whereas the second boundary condition can be shown to be a form of no-normal flow through the boundary.

The solution to Eq. (S10) subject to Eqs. (S11) and (S12) is

$$\tilde{\eta}\left(x\right)=\frac{k\exp\left(kx\right)+\kappa\exp\left(-\kappa x\right)}{k^{2}-\kappa^{2}}\left[-\frac{k}{\rho g}p_{0}-i\frac{k}{\sigma}q_{0}+\frac{1}{\rho gH}\pi_{0}+\frac{f}{\rho gH}\left(\frac{\gamma+i\sigma}{\gamma^{2}+\sigma^{2}}\right)\tau_{0}\right]. \tag{S13}$$

which, at the coast, simplifies to

$$\tilde{\eta}\left(x=0\right)=\frac{1}{k-\kappa}\left[-\frac{k}{\rho g}p_{0}-i\frac{k}{\sigma}q_{0}+\frac{1}{\rho gH}\pi_{0}+\frac{f}{\rho gH}\left(\frac{\gamma+i\sigma}{\gamma^{2}+\sigma^{2}}\right)\tau_{0}\right]. \tag{S14}$$

Adding iq_0/σ to convert from effective sea level to sea level [cf. Eq. (S7)] and scaling by $\exp\left(-i\sigma t\right)$, we obtain the time-variable coastal sea-level solution

$$\zeta\left(x=0,t\right)=\frac{1}{k-\kappa}\left[-\frac{k}{\rho g}p-i\frac{\kappa}{\sigma}q+\frac{1}{\rho gH}\pi+\frac{f}{\rho gH}\left(\frac{\gamma+i\sigma}{\gamma^{2}+\sigma^{2}}\right)\tau\right], \tag{S15}$$

where, on the right side, we understand the forcing terms to be evaluated at the coast.

Recognizing that $i\exp\left(-i\sigma t\right)=\mathcal{H}\left[\exp\left(-i\sigma t\right)\right]$ by definition of the Hilbert transform $\mathcal{H}$, and in analogy with Eq. (1) in the main text, we can write Eq. (S15) equivalently as

$$\zeta\left(x=0,t\right)=a_{\pi}\pi+b_{\pi}\mathcal{H}\left(\pi\right)+a_{\tau}\tau+b_{\tau}\mathcal{H}\left(\tau\right)+a_{p}p+b_{p}\mathcal{H}\left(p\right)+a_{q}q+b_{q}\mathcal{H}\left(q\right), \tag{S16}$$

where

$$a_{\pi}\doteq\Re\left[\frac{1}{k-\kappa}\left(\frac{1}{\rho gH}\right)\right],\ b_{\pi}\doteq\Im\left[\frac{1}{k-\kappa}\left(\frac{1}{\rho gH}\right)\right], \tag{S17}$$

$$a_{\tau}\doteq\Re\left\{\frac{1}{k-\kappa}\left[\frac{f}{\rho gH}\left(\frac{\gamma+i\sigma}{\gamma^{2}+\sigma^{2}}\right)\right]\right\},\ b_{\tau}\doteq\Im\left\{\frac{1}{k-\kappa}\left[\frac{f}{\rho gH}\left(\frac{\gamma+i\sigma}{\gamma^{2}+\sigma^{2}}\right)\right]\right\}, \tag{S18}$$

$$a_{p}\doteq\Re\left[\frac{1}{k-\kappa}\left(-\frac{k}{\rho g}\right)\right],\ b_{p}\doteq\Im\left[\frac{1}{k-\kappa}\left(-\frac{k}{\rho g}\right)\right], \tag{S19}$$

$$a_{q}\doteq\Re\left[\frac{1}{k-\kappa}\left(-i\frac{\kappa}{\sigma}\right)\right],\ b_{q}\doteq\Im\left[\frac{1}{k-\kappa}\left(-i\frac{\kappa}{\sigma}\right)\right], \tag{S20}$$

and where $\Re$ and $\Im$ correspond to real and imaginary parts, respectively.

To evaluate Eqs. (S17)–(S20), we use reasonable, representative numerical values or ranges for the various parameters (Table S2). We assume that σ is between $2\pi/\left(1\text{ day}\right)$

and $2\pi/(6\text{ days})$. This range is selected because roughly two-thirds of the landfalling ARs considered here have lifetimes between 1 and 6 days (not shown).

In Figure S2, we compare numerical values of the various a and b terms determined empirically from ridge regression applied to the data to those values expected theoretically from first principles as embodied in Eqs. (S17)–(S20) and evaluated as described in the previous paragraph. Empirical values are shown as a function of ridge-regression parameter λ and represent 95% confidence intervals across all tide gauges and bootstrap iterations. Theoretical values are shown as minima and maxima based on the parameter values in Table S2 and the target frequency range.

Acknowledging that uncertainties are large, we find that empirical and theoretical coefficients are roughly consistent to order of magnitude, overlapping within their estimated uncertainties (Figure S2). This supports the hypothesis that statistical results in the main text are informative of causal relationships. Note that, in mentioning the rough consistency between empirical and theoretical results, we are not arguing that the analytical model represents all of the relevant physics underlying ζ during ARs. This model framework is highly simplified, and omits many factors that may be important in the real world (e.g., stratification, nonlinearities, alongshore dependence, topographic variation). Our goal here was to identify a simple model based on reasonable assumptions and amenable to analytical solution to show that statistical relationships between forcing and response obtained through regression analysis are not in gross conflict with expectations from basic physics. While we believe we have largely accomplished this goal, we recognize that our results identify open questions. For

example, while the estimates feature overlapping uncertainties, empirical values of a_π are largely negative, whereas first principles predict a positive a_π value (Figure S2 top left). (Keep in mind that, according to regression analysis, π is not an important ζ driver.) We speculate that this discrepancy could reflect unphysical relationships inferred by the regression analysis or important physics not represented in the analytical model. Future studies based on more comprehensive causal frameworks (e.g., high-resolution general circulation models) could revisit these questions to identify more unambiguously the relative roles of different forcing mechanisms and the nature of the oceanic response.

References

Efron, B., & Hastie, T. (2016). Computer Age Statistical Inference: Algorithms, Evidence, and Data Science. Cambridge University Press, Cambridge, 475 pp.

Gill, A. E. (1982). Atmosphere-Ocean Dynamics. Academic Press, San Diego, 662 pp.

Ponte, R. M. (2006). Oceanic Response to Surface Loading Effects Neglected in Volume-Conserving Models. *Journal of Physical Oceanography*, *36*, 426–434, https://doi.org/10.1175/JPO2843.1.

Station	ID	Latitude	Longitude	Completeness	Threshold (cm)	99.5th Percentile (cm)
San Diego	9410170	32.7°N	117.2°W	99.2%	57.0	37.8
La Jolla	9410230	32.9°N	117.3°W	99.7%	56.5	36.3
Los Angeles	9410660	33.7°N	118.3°W	100.0%	56.7	36.0
Santa Monica	9410840	34°N	118.5°W	91.4%	56.6	37.0
Port San Luis	9412110	35.2°N	120.8°W	99.5%	56.5	32.4
Monterey	9413450	36.6°N	121.9°W	99.7%	56.5	31.7
Alameda	9414750	37.8°N	122.3°W	99.8%	58.0	27.4
San Francisco	9414290	37.8°N	122.5°W	99.8%	57.1	28.1
Point Reyes	9415020	38.0°N	123.0°W	98.9%	57.0	32.5
Port Chicago	9415144	38.1°N	122.0°W	98.5%	56.0	26.9
Arena Cove	9416841	38.9°N	123.7°W	78.8%	57.2	34.8
Humboldt Bay	9418767	40.8°N	124.2°W	98.4%	58.4	37.7
Crescent City	9419750	41.7°N	124.2°W	98.8%	58.4	36.0
Port Orford	9431647	42.7°N	124.5°W	87.2%	58.9	39.3
Charleston	9432780	43.3°N	124.3°W	98.5%	59.3	40.5
South Beach	9435380	44.6°N	124.0°W	99.3%	60.2	43.3
Astoria	9439040	46.2°N	123.8°W	99.3%	60.5	44.4
Toke Point	9440910	46.7°N	124.0°W	92.2%	60.9	51.1
Seattle	9447130	47.6°N	122.3°W	100.0%	63.8	34.9
Port Townsend	9444900	48.1°N	122.8°W	99.6%	60.4	36.3
Port Angeles	9444090	48.1°N	123.4°W	98.8%	58.6	41.5
Neah Bay	9443090	48.4°N	124.6°W	99.7%	59.7	46.0
Friday Harbor	9449880	48.5°N	123.0°W	99.9%	59.5	39.1
Cherry Point	9449424	48.9°N	122.8°W	98.5%	61.2	37.2

Table S1. Name, identification number, latitude, longitude, completeness, HTF threshold, and 99.5th percentile of tide-gauge stations and their hourly still water level records during 1980–2016. Identification numbers are as provided by NOAA. Completeness refers to the percentage of hours during the study period for which the tide gauge returned valid hourly still water level data. HTF threshold is a linear function of great diurnal range (difference between mean higher high water and mean lower low water) after Sweet et al. (2018). Values for HTF threshold and 99.5th percentile are relative to mean higher high water. Note that the Humboldt Bay tide gauge is also known as North Spit.

Parameter	Description	Value
ζ	Sea Level	—
η	Effective Sea Level	—
u	Onshore Velocity	—
v	Alongshore Velocity	—
τ	Meridional Wind Stress	—
π	Zonal Wind Stress	—
q	Precipitation	—
p	Barometric Pressure	—
t	Time	—
x	Onshore Coordinate	—
σ	Angular Frequency	—
ρ	Ocean Density	1000 kg m^{-3}
g	Gravitational Acceleration	10 m s^{-2}
k	Offshore Decay Scale	50–200 km
H	Shelf Depth	100–200 m
f	Coriolis Parameter	0.6–1.1$\times 10^{-4}$ s^{-1}
r	Friction Coefficient	1×10^{-4}–1×10^{-2} m s^{-1}
γ	Inverse Frictional Timescale	5×10^{-7}–1×10^{-4} s^{-1}

Table S2. Analytical model variables and parameters. Reasonable parameter values and ranges are given where applicable.

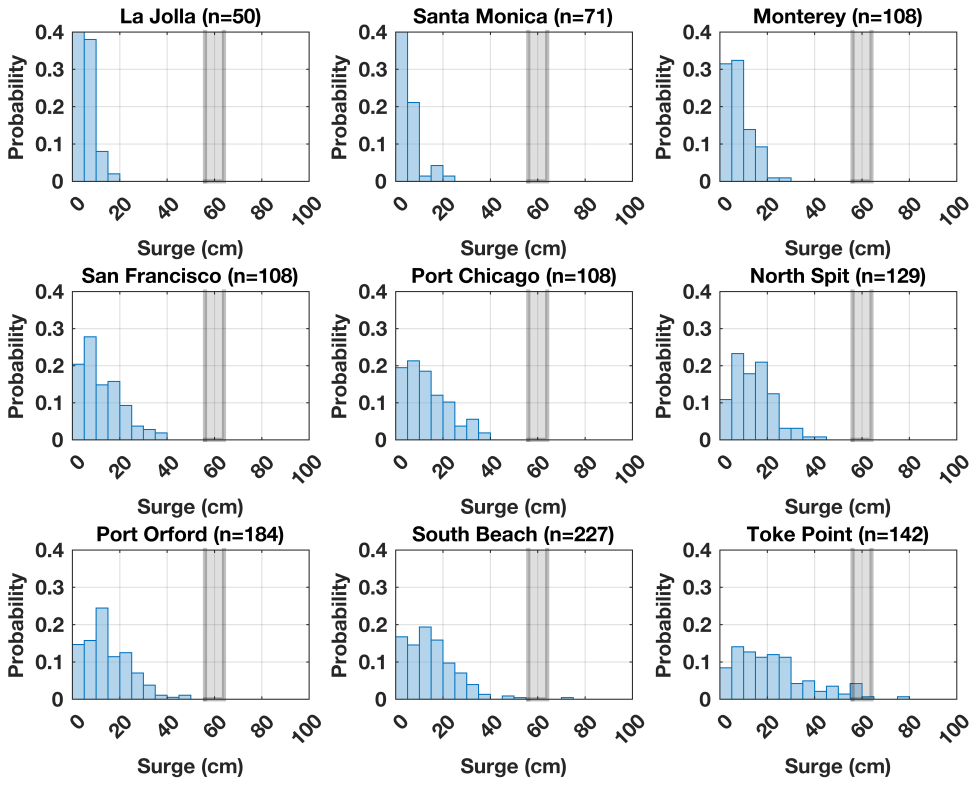

Figure S1. Blue shading shows probability density functions of surges during ARs at example tide gauges (location names and number of AR events identified in the title of each panel). For reference, gray shading identifies the 56–64-cm range that encompasses the HTF thresholds (above mean higher high water) at the tide gauges (cf. Table S1).

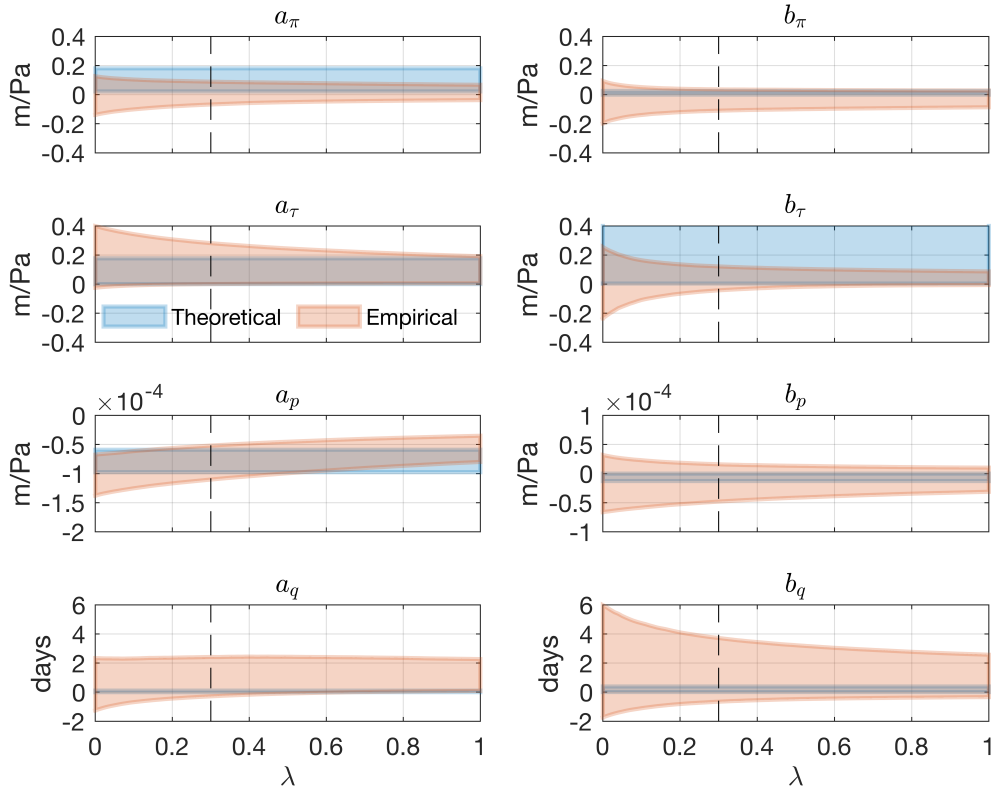

Figure S2. Coefficients between atmospheric forcing and storm surge ζ found empirically from regression analysis (orange) and expected theoretically from the analytical model (blue). Left column shows coefficients between ζ and atmospheric forcing [a's in Eqs. (1), (S16)–(S20)], whereas right column shows coefficients between ζ and the Hilbert transforms of atmospheric forcing [b's in Eqs. (1), (S16)–(S20)]. First row shows results for zonal wind stress π, second row meridional wind stress τ, third row barometric pressure p, and fourth row precipitation q. Empirical values are 95% confidence intervals across all sites as a function of ridge-regression parameter λ (vertical black dashes identify $\lambda = 0.3$). Theoretical values are shown as min/max ranges based on Eqs. (S16)–(S20) evaluated using parameter values/ranges in Table S2 and an angular frequency σ range between $2\pi/\,(1\text{ day})$ and $2\pi/\,(6\text{ days})$.

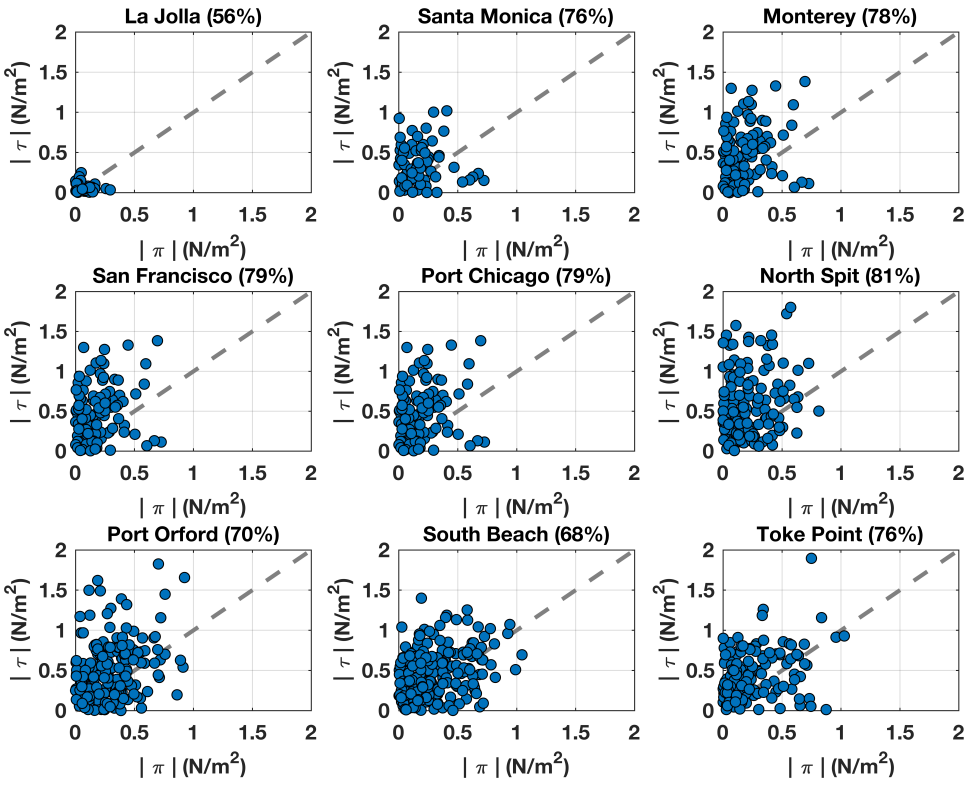

Figure S3. Blue dots compare magnitudes of high-pass-filtered anomalous daily zonal wind stress π (horizontal axes) and meridional wind stress τ (vertical axes) during ARs at example tide gauges (location names and percentages of ARs for which τ magnitudes are larger than π magnitudes identified in the title of each panel). For reference, grey dashes mark the 1:1 line.